

This manuscript is a non-peer reviewed preprint submitted to EarthArXiv.
This manuscript has been submitted for publication in Earth and Planetary Science Letters,
and is currently undergoing peer-review.

Highlights

Can spinodal decomposition occur during decompression-induced vesiculation of magma?

Mizuki Nishiwaki

- Magma vesiculation during decompression was interpreted by simple thermodynamics.
- Binodal and spinodal curves of silicate–water systems were drawn versus pressure.
- Magma vesiculation probably occurs by nucleation, not by spinodal decomposition.
- Spinodal pressure can contribute to an easy estimate of bubble surface tension.

Can spinodal decomposition occur during decompression-induced vesiculation of magma?

Mizuki Nishiwaki^a

^a*Center for Glass Science & Technology, School of Engineering, The University of Shiga Prefecture, 2500, Hassaka-cho, Hikone, Shiga, 522-8533, Japan*

Abstract

Volcanic eruptions are driven by decompression-induced vesiculation of supersaturated volatile components in magma. The initial phase of this phenomenon has long been described as a process of nucleation and growth. Recently, it was proposed that spinodal decomposition (an energetically spontaneous phase separation that does not require the formation of a distinct interface) may occur during decompression-induced magma vesiculation. This suggestion has attracted considerable attention, but is currently only based on textural observations of decompression experiment products (the independence of bubble number density on decompression rate; the homogeneous spatial distribution of the bubbles). In this study, I used a simple thermodynamic approach to investigate whether spinodal decomposition can occur during the decompression-induced vesiculation of magma. I drew the binodal and spinodal curves on the chemical composition–pressure plane by approximating hydrous magmas at several conditions of temperature and chemical composition as two-component symmetric regular solutions of silicate and water, and using experimentally

determined values of water solubility in these magmas. The spinodal curve was much lower than the binodal curve for all the magmas at pressures sufficiently below the second critical endpoint. In addition, the final pressure of all the decompression experiments performed to date fell between these two curves. This suggests that spinodal decomposition is unlikely to occur in the pressure range of magmatic processes in the continental crust, and that decompression-induced magma vesiculation results from nucleation and subsequent growth, as previously considered. In addition, it is expected that by substituting the determined spinodal pressure into the formula of non-classical nucleation theory, the surface tension between the silicate melt and bubble nucleus can be easily estimated.

Keywords: hydrous magma, vesiculation, nucleation, spinodal decomposition, thermodynamics, regular solution

1. Introduction

Magma degassing is one of the strongest controlling factors in the dynamics of volcanic eruptions. Volatiles (e.g., H₂O, CO₂, H₂S) initially dissolved in magma deep underground become insoluble under decompression, precipitating as vapor (bubbles). Understanding this magma vesiculation process is crucial because it dramatically influences eruption style and volcanic explosivity, playing a key role in determining the time evolution of eruptions, ranging from effusive lava flows to highly explosive pyroclastic events. In particular, water often makes up a large

proportion of the various volatile components, and its degassing—in a 10
precise sense, the phase separation into silicate melt saturated with water 11
and supercritical water vapor saturated with trace amounts of silicate—has 12
been extensively studied since Verhoogen (1951). The initial degassing 13
stage has long been understood as nucleation and growth (e.g., Shimozuru 14
et al., 1957; Murase and McBirney, 1973; Sparks, 1978), and theoretical 15
numerical models were constructed by Toramaru (1989, 1995) to predict 16
the bubble number density (BND) based on classical nucleation theory 17
(CNT, e.g., Hirth et al., 1970). In addition, in the last 30 years since 18
the innovative work by Hurwitz and Navon (1994), many experiments 19
have been conducted to reproduce decompression-induced vesiculation of 20
mainly water-dissolved (hydrous) magmas in laboratory experimental magma 21
analogues with controlled decompression rates. As data from decompression 22
experiments to date generally agreed with numerical predictions (BND 23
 $\propto |\text{decompression rate}|^{1.5}$ by Toramaru, 1995) based on CNT, Toramaru 24
(2006) constructed the BND decompression rate meter (BND decompression 25
rate meter). This equation is approximately valid for both homogeneous 26
nucleation of spherical bubbles in a uniform melt (where σ is large) and 27
heterogeneous nucleation of bubbles on crystal surfaces such as Fe–Ti oxides 28
(where σ is small) by applying appropriate corrections to the surface tension 29
 σ between the melt and bubble nucleus (Shea, 2017; Toramaru, 2022). 30
This theoretical model has been used extensively to estimate magma’s 31
decompression rate in a volcanic conduit based on quantitative analysis 32

of bubble texture in natural pyroclastic products (e.g., Toramaru, 2006; 33
Giachetti et al., 2010; Houghton et al., 2010; Nguyen et al., 2014). 34

However, some laboratory experiments performed thus far have reported 35
results that are anharmonic to the above equations; Allabar and Nowak 36
(2018) performed decompression experiments on hydrous phonolitic melts 37
over a wide range of decompression rates, including 0.024–1.7 MPa/s, 38
and found systematically high BND values (5.2 mm^{-3}) independent of 39
decompression rate. To explain this result, they proposed a scenario 40
in which spinodal decomposition, rather than nucleation as used in 41
previous explanations, occurs in the early stages of decompression-induced 42
vesiculation. Spinodal decomposition is the phase separation of a 43
multi-component mixture or solid solution due to energetic instability (e.g., 44
Cahn and Hilliard, 1959; Cahn, 1965). When the system’s temperature, 45
pressure, and chemical composition (T, P, X) are within the miscibility 46
gap, whether nucleation or spinodal decomposition occurs is determined 47
by the sign of the second-order derivative of the system’s molar Gibbs 48
energy of mixing g^{real} . If the sign is positive, the system is metastable, 49
and nucleation occurs, with distinct phase boundaries (interfaces) appearing 50
spatially random from the beginning. Conversely, if the sign is negative, 51
the system becomes unstable, and spinodal decomposition occurs, in which 52
initially small concentration fluctuations with an unclear phase boundary 53
gradually grow and eventually lead to the separation of two phases at a 54
specific wavelength, forming a distinct interface. The diffusion coefficient is 55

proportional to the second-order derivative of g^{real} , so nucleation corresponds 56
to downhill diffusion, where diffusion progresses in the direction that weakens 57
the concentration gradient. In contrast, spinodal decomposition corresponds 58
to uphill diffusion, where diffusion progresses in the direction that strengthens 59
the concentration gradient (Haasen, 1996). In Allabar and Nowak (2018), 60
spinodal decomposition was proposed for two reasons: (1) the timescale 61
for spinodal decomposition in gas–liquid systems is much shorter than the 62
timescale for decompression (Debenedetti, 2000), which could explain the 63
absence of dependence on BND on the decompression rate. (2) The bubble 64
spatial distribution in the experimental products was homogeneous; the 65
vitrified silicate melt and bubbles appeared to phase-separate at a specific 66
wavelength. Subsequent work by Sahagian and Carley (2020) raised the 67
problem that “the surface tension between the melt and tiny bubble nucleus 68
should act to push dissolved volatiles back into the melt, but bubbles of 69
such size are still formed” and discussed this process as the “tiny bubble 70
paradox.” They extended the ideas of Allabar and Nowak (2018) as follows: 71
if spinodal decomposition—rather than nucleation—occurs, this paradox can 72
be resolved because interface formation is no longer necessary and explains 73
the homogeneous spatial distribution of bubbles observed in some laboratory 74
products. 75

Thus, the new theory that “decompression-induced vesiculation of magma 76
can occur not only by nucleation but also by spinodal decomposition” 77
has been actively discussed and has attracted much attention in the last 78

seven years. Gardner et al. (2023) also stated that future interpretations 79
of BND and bubble size distributions of natural volcanic products must 80
consider the possibility that various mechanisms of bubble formation may 81
occur, including nucleation (homogeneous and heterogeneous) and spinodal 82
decomposition. However, whether spinodal decomposition actually occurs 83
during decompression-induced magma vesiculation remains speculative. 84
Nonetheless, owing to the small spatiotemporal scale of the physical 85
phenomena under investigation, it is likely to be extremely difficult to 86
confirm via laboratory observational experiments. Therefore, in this paper, 87
I discuss which nucleation or spinodal decomposition mechanism is likely to 88
occur during decompression-induced magma vesiculation, based on a simple 89
thermodynamic approach. 90

This study first reviews the thermodynamic definitions of nucleation and 91
spinodal decomposition. Spinodal decomposition, which has traditionally 92
been treated when it occurs with a change in temperature at constant 93
pressure, can also be treated with a change in pressure at constant 94
temperature. An attempt is made to consider hydrous magmas in a 95
simplified way as a symmetric regular solution of silicate and water 96
and to draw binodal and spinodal curves quantitatively on the chemical 97
composition–pressure plane using a simple calculation. Next, based on 98
the calculation results, I discussed the possibility of spinodal decomposition 99
occurring in decompressing magma. Furthermore, I provided insights on the 100
kinetic effects that should be considered in real systems and how the results 101

of previous decompression experiments should be interpreted about the BND 102
decompression rate meter. Finally, as a potential application of the model 103
proposed in this study, an estimate of the surface tension between the melt 104
and the bubble nucleus was presented. 105

2. Energetics on the mixing of silicate and water 106

2.1. General theory: Thermodynamic energetics of two-component mixture 107

Notations used in this study are listed in Table 1. Here, I will explain the 108
thermodynamics of a two-component mixture. In general, the molar Gibbs 109
energy of a mixture, g^{real} , is described as the sum of the ideal solution's 110
Gibbs energy, g^{ideal} (which arises from configurational entropy), and the 111
excess energy, g^{excess} ($\neq 0$, represents the deviation from the ideal solution) 112
(e.g., Guggenheim, 1952): 113

$$g^{\text{real}} = g^{\text{ideal}} + g^{\text{excess}}, \quad (1)$$

where the amount obtained by proportionally distributing and summing the 114
Gibbs energies of each pure phase is subtracted as the baseline. In an ideal 115
solution, $g^{\text{excess}} = 0$. Several types of non-ideal solutions that take into 116
account the deviation from the ideal solution, $g^{\text{excess}} \neq 0$; among them, the 117
most basic type is the regular solution. In a regular solution, the non-ideal 118
entropy is neglected ($s^{\text{excess}} = 0$), and the non-ideal enthalpy is treated as 119
 $h^{\text{excess}} \neq 0$, which leads to the relationship $g^{\text{excess}} = h^{\text{excess}}$. Here, x represents 120

the mole fraction of one of the components ($0 < x < 1$). In this case, as 121
 explained below, g^{ideal} is always symmetric with respect to $x = 0.5$, while the 122
 shape of g^{excess} (and g^{real}) is assumed to be either symmetric or asymmetric. 123
 The g^{ideal} at a given temperature T is expressed by the following equation. 124

$$g^{\text{ideal}} = RT\{x \ln x + (1 - x) \ln(1 - x)\}. \quad (2)$$

The equation for g^{excess} differs depending on whether the symmetric or 125
 asymmetric model. In the case of the symmetric model, 126

$$g^{\text{excess}} = x(1 - x)w_{\text{sym}}, \quad (3)$$

where w_{sym} is the interaction parameter between the two components A and 127
 B, representing the non-ideality of mixing. In the case of the asymmetric 128
 model, 129

$$g^{\text{excess}} = x(1 - x)\{w_A(1 - x) + w_Bx\}, \quad (4)$$

where w_A and w_B are the interaction parameters when a particle of A enters a 130
 group of B, and when a particle of B enters a group of A, respectively. These 131
 represent the slopes of the g^{excess} curve at the endpoints on the B side and A 132
 side, where a positive slope indicates that the system becomes energetically 133
 unstable after mixing. In contrast, a negative slope indicates that the system 134
 becomes energetically stable. Based on this, the Gibbs energy curves for 135
 both the symmetric and asymmetric models are illustrated as shown in Fig. 136

1. Here, we assume that for the symmetric model, $w_{\text{sym}} > 0$, and for the 137
asymmetric model, $w_A > 0$ and $w_B > 0$. 138

The g^{real} curve for the symmetric model and its corresponding phase 139
diagram are shown in Fig. 2. Hereafter, we focus on conditions under which 140
the system's temperature, pressure, and chemical composition (T, P, X) lie 141
within the miscibility gap. Compositions outside the two local minima of 142
the g^{real} curve correspond to a single-phase system, while compositions inside 143
these minima undergo phase separation into a two-phase system. In other 144
words, the point where the first derivative of the g^{real} curve with respect to x 145
equals zero corresponds to the one-phase/two-phase boundary in the phase 146
diagram (i.e., the binodal curve). In the region between the local minimum 147
and the inflection point, where the g^{real} curve is convex downwards (i.e., 148
where the second-order derivative with respect to x is positive), the system is 149
metastable, and nucleation occurs with distinct phase boundaries (interfaces) 150
appearing randomly in space. Conversely, in the interval where the g^{real} curve 151
is convex upward, i.e., where the sign of the second-order derivative with x is 152
negative, the system is unstable, and spinodal decomposition occurs wherein 153
the two phases start to separate at a specific wavelength with unclear phase 154
boundaries. In other words, the point where the second derivative of the 155
 g^{real} curve with respect to x equals 0 corresponds to the nucleation/spinodal 156
decomposition boundary (i.e., the spinodal curve) in the phase diagram. 157

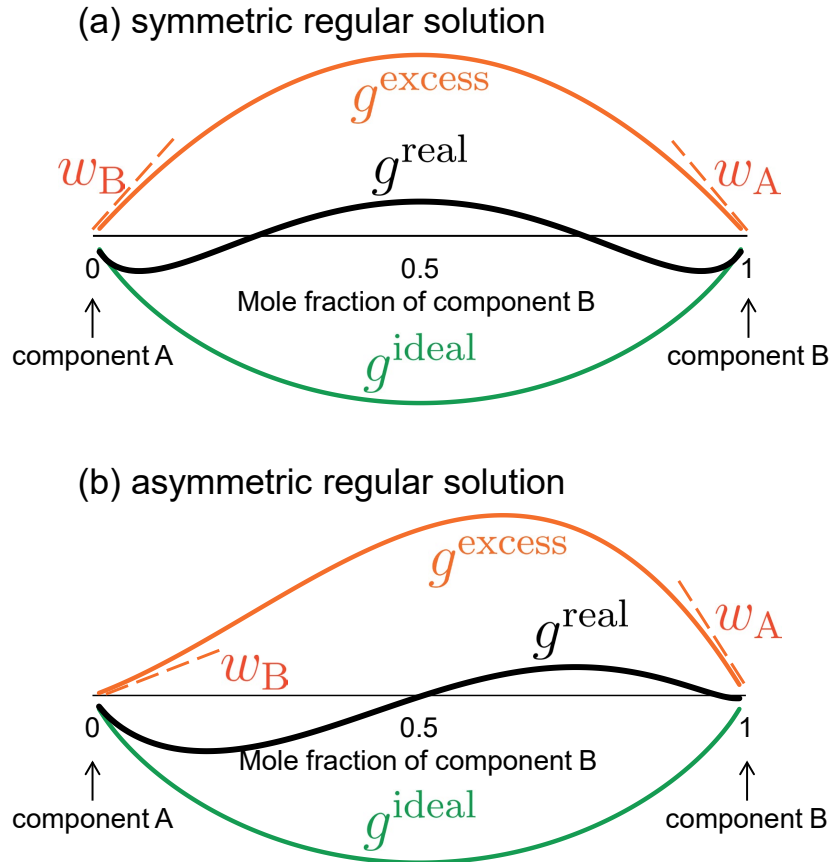


Figure 1: Schematic diagrams of the molar Gibbs energy for regular solutions of two components A and B: (a) symmetric regular solution and (b) asymmetric regular solution. The green curve represents that of an ideal solution g^{ideal} , which is common to both regular solution models. The orange curve represents the molar excess Gibbs energy for a regular solution g^{excess} , and the two models are differentiated based on its shape. The bold black curve represents the sum of these: the molar Gibbs energy of mixing g^{real} . The interaction parameters w_A and w_B are represented by the slopes of the g^{excess} curve at the endpoints on the B side and A side, respectively. In the symmetric model (a), $w_A = w_B$, which is referred to as w_{sym} in the text.

Mathematically, for the symmetric model,

158

$$\left(\frac{\partial g^{\text{real}}}{\partial x}\right)_{T,P} = RT \ln\left(\frac{x}{1-x}\right) + (1-2x)w_{\text{sym}}, \quad (5)$$

$$\left(\frac{\partial^2 g^{\text{real}}}{\partial x^2}\right)_{T,P} = \frac{RT}{x(1-x)} - 2w_{\text{sym}}, \quad (6)$$

and for the asymmetric model,

159

$$\left(\frac{\partial g^{\text{real}}}{\partial x}\right)_{T,P} = RT \ln\left(\frac{x}{1-x}\right) + w_{\text{A}}x(2-3x) + w_{\text{B}}(3x^2-4x+1), \quad (7)$$

$$\left(\frac{\partial^2 g^{\text{real}}}{\partial x^2}\right)_{T,P} = \frac{RT}{x(1-x)} + 2\{w_{\text{A}}(1-3x) + w_{\text{B}}(3x-2)\}, \quad (8)$$

the solutions x when these equations are equal to 0 form the binodal and spinodal curves. Binodal and spinodal curves appear on the cut surfaces of binodal and spinodal surfaces in temperature–pressure–chemical composition space (e.g., Aursand et al., 2017). Hence, either temperature or pressure can be selected for the vertical axis in the lower panel of Fig. 2. This will be explained in section 2.3.

It is well known that silicate melts, which are mixtures of multiple types of oxides, can separate into several distinct phases depending on changes in temperature and pressure, both in natural and industrial compositions: for example, liquid–liquid separation as seen in James (1975); Charlier and Grove (2012). Dehydration of magma is no exception and can be viewed as a separation into liquid phase (water-saturated silicate melt) and vapor phase (silicate-saturated water vapor), i.e., liquid–vapor separation. In this

study, hydrous magma is approximated as a regular solution consisting of 173
two components: anhydrous silicate (melt) and water (vapor), and the 174
thermodynamics of mixing these two components is considered. Therefore, in 175
the following, components A and B are taken to represent silicate and water, 176
respectively. Note that water in magma exists as two molecular species: the 177
molecule H_2O_m and the hydroxyl groups OH (e.g., Stolper, 1982a; 1982b), 178
but we consider them together here. That is, x is the mole fraction of total 179
water. Notably, at and near the silicate end member, a crystalline phase 180
precipitates at low temperatures (e.g., Fig. 4 in Ostrovsky, 1966 for the 181
 $\text{SiO}_2\text{-H}_2\text{O}$ system; Fig. 7 in Paillat et al., 1992; and Fig. 3 in Makhluif et 182
al., 2020 for the albite- H_2O system); however, in this study, it is neglected, 183
assuming the amount to be minute and the system to be at a sufficiently 184
high temperature for this assumption to hold, for simplicity. 185

2.2. Regular solution approximation 186

2.2.1. Symmetric model vs. asymmetric model 187

We will consider which model, symmetric or asymmetric, is more 188
appropriate for approximating hydrous magma as a two-component regular 189
solution in the silicate-water system, based on both observational and 190
experimental facts about the behavior of real systems and the mathematical 191
convenience of the models. First, we will discuss the relationship between 192
 x_{bi} and x_{spi} for each model. In particular, to later utilize knowledge on the 193
silicate-rich side (e.g., the solubility of water in magma), we will focus on the 194

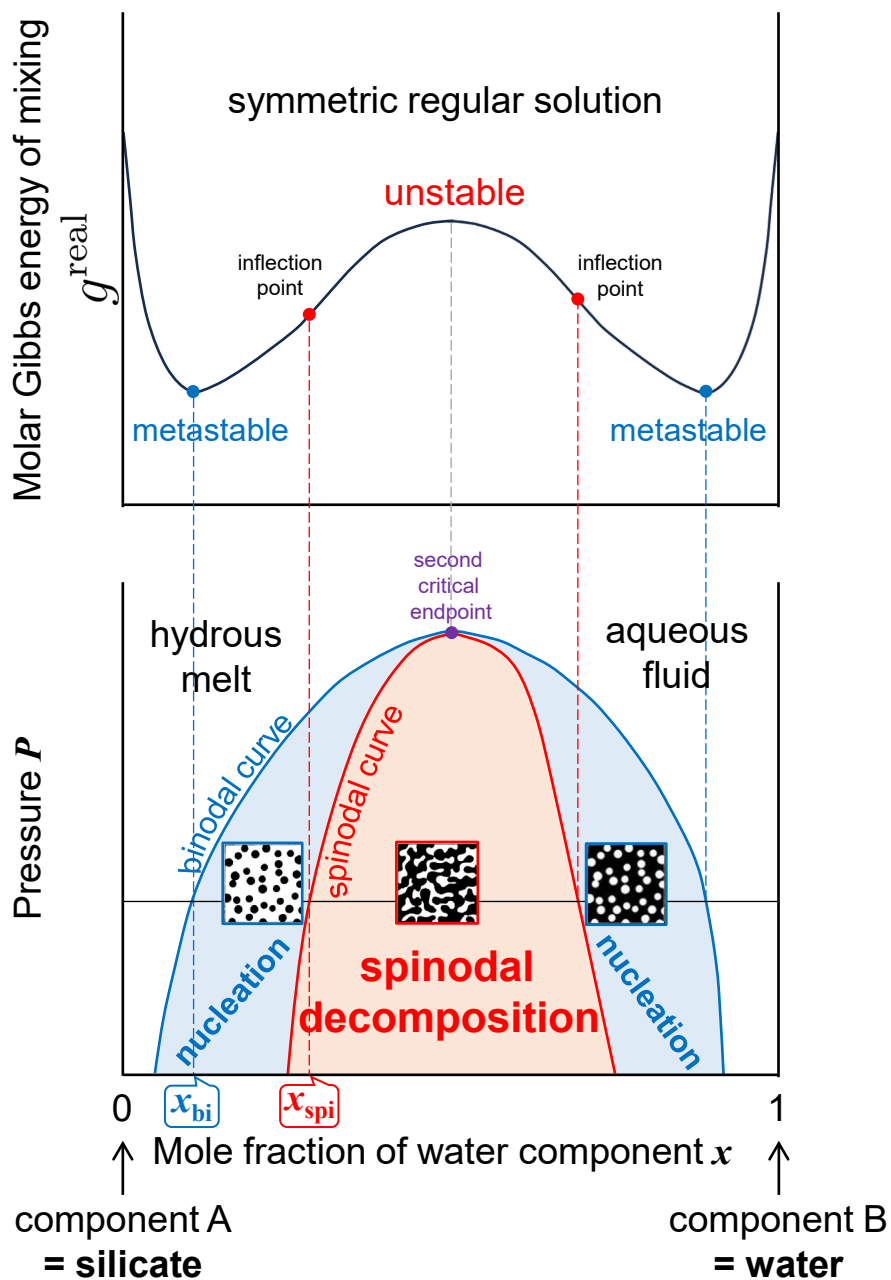


Figure 2: Schematic molar Gibbs energy of mixing g^{real} (upper panel) and corresponding phase diagram (lower panel) for a general two-component symmetric regular solution. In the interval where the g^{real} curve is convex downwards, the system is metastable, and nucleation occurs with clear phase boundaries (surfaces) appearing randomly in space. On the other hand, when the g^{real} curve is convex upward, the system is unstable, and spinodal decomposition occurs, in which the two phases start to separate at a specific wavelength with unclear phase boundaries. 13

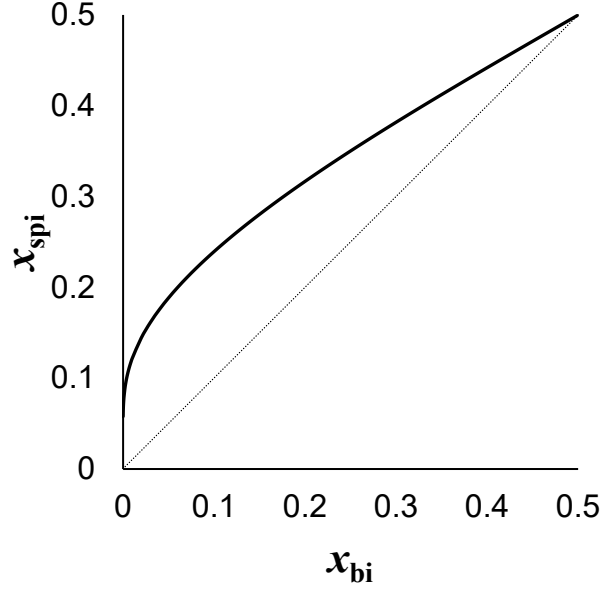


Figure 3: The relation between x_{bi} and x_{spi} at an arbitrary fixed temperature, derived from a series of Eqs. (5) and (6), which represent the first- and second-order derivatives of g^{real} by x . x_{bi} and x_{spi} are the x values that constitute the binodal and spinodal curves, respectively. The range $0 < x < 0.5$ corresponds to the left half of Fig. 1. The relation $x_{\text{spi}} > x_{\text{bi}}$ holds for all the ranges.

range of x smaller than the x at which g^{real} reaches its maximum. 195

For the symmetric model, combining Eqs. (5) and (6) and eliminating 196
 w_{sym} , the following relation between x_{bi} and x_{spi} is derived: 197

$$x_{\text{spi}} = \frac{1}{2} \left\{ 1 - \sqrt{1 - \frac{2(1 - 2x_{\text{bi}})}{\ln \frac{1 - x_{\text{bi}}}{x_{\text{bi}}}}} \right\}. \quad (9)$$

This relation is shown in Fig. 3 in the $0 < x < 0.5$ range, corresponding to 198
the left half area of Fig. 2. 199

On the other hand, in the asymmetric model, the signs of the slopes at 200

both ends of the g^{excess} , i.e., w_A and w_B , are important. When combining 201
 Eqs. (7) and (8), if both w_A and w_B are positive, the relationship between 202
 x_{bi} and x_{spi} at a given T or P will be a one-to-one correspondence, just like 203
 in the symmetric model. As is well-known, the silicate–water system has 204
 a large miscibility gap (e.g., Kennedy, 1962; Paillat et al., 1992; Shen and 205
 Keppler, 1997; Bureau and Keppler, 1999), so it is necessary for $g^{\text{excess}} >$ 206
 0 over a wide range of x . Therefore, the assumption that both $w_A >$ 207
 $w_B >$ 0 seems reasonable. However, this case may not strictly align 208
 with the behavior of real systems. For example, at the silicate-rich side, 209
 when water dissolves, it is slightly exothermic, i.e., $g^{\text{excess}} <$ 0 , as suggested 210
 by HF solution calorimetry of hydrous volcanic glasses synthesized at high 211
 temperature and pressure (Clemens and Navrotsky, 1987; Richet et al., 2004; 212
 2006). If we trust this experimental result, the correct assumption would be 213
 that $w_A >$ 0 and slightly $w_B <$ 0 . In other words, the shape of the g^{excess} (and 214
 thus g^{real}) for hydrous magma is asymmetric, and their peaks should slightly 215
 shift from $x = 0.5$ (Fig. 4 (a)). But then again, in this case, the relationship 216
 between x_{bi} and x_{spi} at a given T or P becomes a complex multivalued 217
 function, as shown in Fig. 4 (b). Specifically, this figure suggests that the 218
 spinodal curve corresponding to x_{bi} in the range $0 < x_{\text{bi}} < 1/3$ intersects 219
 with the spinodal curve corresponding to x_{bi} in the range $2/3 < x_{\text{bi}} < 1$, 220
 which is unrealistic. 221

Thus, the theoretical equations for a two-component asymmetric regular 222
 solution do not fit the actual energy curves of g^{excess} (and g^{real}) well. 223

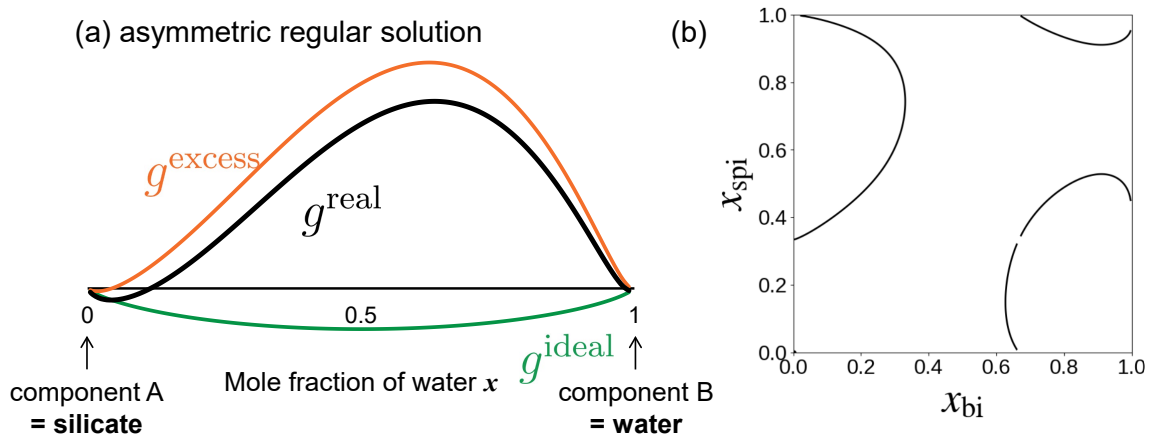


Figure 4: (a) Schematic diagram of the molar Gibbs energy for a realistic hydrous magma, when it was assumed as an asymmetric regular solution of anhydrous silicate (melt) and water (vapor). The meaning of each curve is the same as in Fig. 1. Components A and B correspond to silicate and water, respectively. (b) The relationship between x_{bi} and x_{spi} in a two-component asymmetric regular solution model. An example is shown for the case where $T = 1,000^{\circ}\text{C}$, $w_A = 345.7 \text{ kJ/mol}$, and $w_B = -1.0 \text{ kJ/mol}$.

This issue could be addressed by increasing the number of components 224
to distinguish, thereby increasing the number of unknown interaction 225
parameters w . For example, in the case of a three-component asymmetric 226
regular solution, the expression for g^{excess} can be written as follows (Kakuda 227

$$\begin{aligned}
g^{\text{excess}} &= x_A x_A x_B w_{AAB} & (10) \\
&+ x_A x_B x_B w_{ABB} \\
&+ x_B x_B x_C w_{BBC} \\
&+ x_B x_C x_C w_{BCC} \\
&+ x_C x_C x_A w_{CCA} \\
&+ x_C x_A x_A w_{CAA} \\
&+ 2x_A x_B x_C w_{ABC},
\end{aligned}$$

where w_{ijk} is the interaction parameter between particles in a triplet 229
consisting of three particles. Nishiwaki (2023) distinguished between the 230
molecular species of water (molecular water H_2O_m and hydroxyl groups OH) 231
and considered hydrous magma as a three-component system consisting of 232
bridging oxygen of anhydrous silicate and these water species. Additionally, 233
he attempted to determine the values of the seven w_{ijk} parameters and 234
the shapes of g^{excess} (and g^{real}) over a wide range of temperatures and 235
pressures. However, this problem is highly challenging from a linear algebraic 236
standpoint, and the values reported in Nishiwaki (2023) are likely to be 237
incorrect. We are currently working toward resolving this issue (Nishiwaki 238
and Fukuya, in prep.). In the end, although we know that the shape of g^{excess} 239
(and g^{real}) is complex, as shown in Fig. 4 (a), for now, we have no choice 240

but to compromise and approximate hydrous magma as a two-component
symmetric regular solution consisting of silicate and water. As a result,
this approach is consistent with the scheme adopted by Allabar and Nowak
(2018).

2.2.2. Consistency with known phase diagrams

Next, we will evaluate the validity of the two-component symmetric
regular solution approximation by comparing it with the already-known
phase diagrams. In Fig. 2, the regions on the silicate-rich and water-rich
sides at pressures higher than the binodal curve, correspond to hydrous melt
and aqueous fluid, respectively. Thus, when a pressure change occurs that
cuts the binodal curve at a fixed chemical composition, the reaction “magma
(supercritical fluid) \leftrightarrow water-saturated silicate melt (hydrous melt) + almost
pure water vapor (aqueous fluid)” occurs. The rightward reaction indicates
exsolution with decompression, whereas the leftward reaction indicates
mutual dissolution with compression. For example, according to the results of
high-temperature and high-pressure experiments shown in Fig. 3 of Makhluaf
et al. (2020), for the albite–water system at 900°C, the second critical
endpoint (the vertex of the miscibility gap) is in the range of 1.25–1.40 GPa
and 42–45 wt%, i.e., $x = 0.57$ – 0.60 (on a single oxygen basis). While some
experimental studies have indicated that the position of the second critical
endpoint may vary depending on the temperature and chemical composition
of the silicate (Bureau and Keppler, 1999; Sowerby and Keppler, 2002), in

this study, I assume that it does not deviate significantly from $x = 0.5$ 263
to use the symmetric regular solution approximation, as mentioned in the 264
previous section. This assumption may be somewhat forceful, but it is the 265
simplest model we can present at this stage, and it will serve as a baseline 266
for comparison when the detailed shape of the Gibbs energy is determined 267
in the future, and the model is updated. 268

2.3. Spinodal decomposition with pressure change 269

Since spinodal decomposition is a phenomenon discovered in the 270
field of inorganic materials such as ceramics and alloys (e.g., Cahn, 271
1965), it is typically discussed in terms of phase separation into 272
solid–solid/solid–liquid/liquid–liquid systems that occur with decreasing 273
temperature at normal pressure. Thus, temperature is typically used as the 274
vertical axis when drawing phase diagrams. In contrast, when considering 275
whether spinodal decomposition occurs in the phase separation of magma 276
into gas–liquid systems, I assumed constant temperature and focused on the 277
phase separation that occurs during decompression, since water solubility is 278
much more dependent on pressure than temperature. Therefore, I adopted 279
pressure as the vertical axis in the phase diagram in Fig. 2. It has 280
been suggested that, in nature, magma degassing may be more efficiently 281
achieved through heating caused by the latent heat of crystallization, 282
viscosity, and friction rather than decompression (e.g., Lavalée et al., 2015). 283
However, typically, decompression experiments are conducted at a constant 284

temperature, and so far, scenarios of spinodal decomposition have been 285
proposed based solely on the results of such experiments (Gonnermann and 286
Gardner, 2013; Allabar and Nowak, 2018; Allabar et al., 2020b; Sahagian 287
and Carley, 2020; Gardner et al., 2023; Marks and Nowak, 2024; Hummel et 288
al., 2024). Therefore, focusing on the pressure direction to test the validity 289
of this scenario is not necessarily a flawed assumption. 290

3. Calculation methods 291

3.1. Relation between water solubility curve and binodal curve, and 292 calculation of the spinodal curve 293

The section for $x < 0.5$ of the binodal curve on the x - P plane at constant 294
 T , shown in the lower panel of Fig. 2, should coincide with the solubility 295
curve of water in the silicate melt at that temperature with respect to pressure 296
change. In other words, the water solubility $c(P)$ in the silicate melt is equal 297
to $x_{\text{bi}}(P)$, which constitutes the binodal curve. From this and the relation Eq. 298
(9) between x_{bi} and x_{spi} , we can calculate the value of x_{spi} that constitutes 299
the spinodal curve. The value of the silicate–water interaction parameter 300
 $w_{\text{sym}}(P)$ at a fixed temperature can also be determined by substituting the 301
value of $x_{\text{bi}}(P)$ into Eq. (5) or the value of $x_{\text{spi}}(P)$ into Eq. (6). 302

3.2. Conditions on the temperature, chemical composition, and water 303 solubility in magma 304

Three types of silicate melts are assumed for temperature and chemical 305
composition: K-phonolitic melt at 1,050°C, basaltic melt at 1,100°C, and 306

albite melt at 900°C. For the phonolitic melt, the conditions are the 307
same as those used in all experiments of Allabar and Nowak (2018). 308
Basaltic and albite melts were chosen to compare and examine the spinodal 309
curves' behavior at higher pressures. The temperatures employed are those 310
at which the pressure dependence of water solubility in the melt was 311
already systematically determined from high-temperature and high-pressure 312
experiments. According to Iacono-Marziano et al. (2007), who performed 313
decompression experiments using AD79 Vesuvius pumice as did Allabar and 314
Nowak (2018), since the water solubility in K-rich phonolitic melt at 1,050°C 315
agrees well with the value calculated from the empirical model of Moore et 316
al. (1998), their formula was also used in this study in the range 0.1–300 317
MPa. Note that Moore et al. (1998) defined the mole fraction of water by 318
treating each oxide (e.g., SiO₂ and Al₂O₃) as one unit, but this definition is 319
no longer in common use, and here, the mole fraction was converted to the 320
currently commonly used single-oxygen basis values (see Section 1.2 in Zhang, 321
1999). The water solubility in the basaltic melt at 1,100°C was obtained by 322
digitizing the fitting curve of the experimentally determined values for \lesssim 600 323
MPa, as shown in Fig. 2 of Hamilton et al. (1964). The water solubility in 324
the albite melt at 900°C was also obtained by digitizing the fitting curve of 325
the experimentally determined values for \lesssim 1000 MPa, as shown in Fig. 8 of 326
Burnham and Jahns (1962). 327

4. Calculation results

328

The binodal and spinodal curves drawn on the x - P plane for the three 329
silicate-water systems are shown in Fig. 5. The geometric characteristics 330
of both curves are similar, regardless of the silicate composition. Fig. 6 in 331
Allabar and Nowak (2018) and Fig. 1 in Sahagian and Carley (2020) show a 332
conceptual phase diagram in which both the binodal and spinodal curves are 333
convex upward over the entire chemical composition range, with a large area 334
inside the spinodal curve. The lower panel of Fig. 2 in this study is identical. 335
However, when considering their actual position and shape quantitatively 336
based on chemical thermodynamics, the solubility curve (= binodal curve) 337
is convex downward at $\lesssim 400$ MPa (approximately the relation $c(P) \propto P^{0.5}$ 338
holds); therefore, the spinodal curve is also convex downward. In the pressure 339
range examined in this study, the spinodal curve is situated at a much lower 340
pressure relative to the binodal curve when fixed at a certain water content. 341
For example, at $x = 0.10$, the water solubility (wt%), P_{bi} (MPa), and P_{spi} 342
(MPa) for the phonolitic melt, basaltic melt, and albite melt are (5.4, 219, 343
< 1), (5.2, 239, 6), and (5.8, 166, 10), respectively. Furthermore, as x 344
increases, the corresponding P_{spi} gradually transitions to the high-pressure 345
side, but the difference from P_{bi} is still very large. In other words, the 346
nucleation region is much broader than the spinodal decomposition region, 347
at least in the $x < 0.25$ range plotted in Fig. 5. For example, in the case of 348
albite melt, $P_{\text{bi}} = 1000$ MPa, which corresponds to approximately $P_{\text{spi}} = 190$ 349
MPa. 350

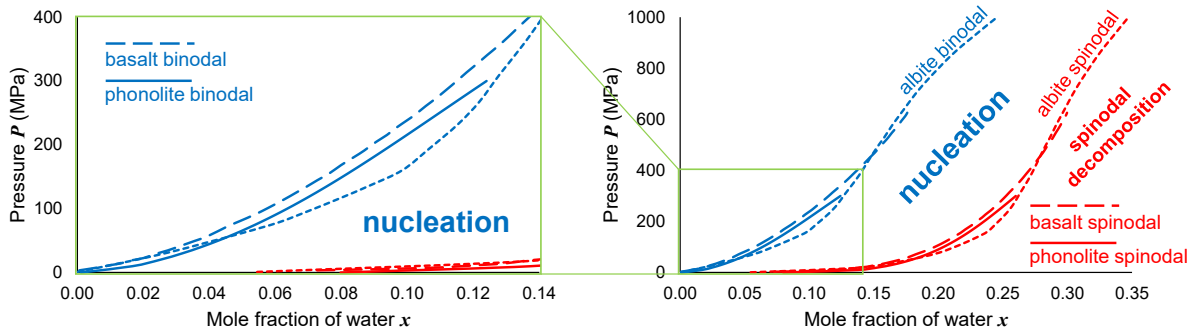


Figure 5: Binodal (blue) and spinodal (red) curves for hydrous 1,050°C K-phonolitic (solid line), 1,100°C basaltic (dashed line), and 900°C albite (dotted line) melts in the pressure range 0.1–1000 MPa. The left panel shows an enlargement of the right panel at pressures below 400 MPa. The binodal curves correspond to the water solubility curves in the melt for each chemical composition (Moore et al., 1998; Hamilton et al., 1964; Burnham and Jahns, 1962). The position of spinodal curves was determined from the position of binodal curves and Eq. (9).

The calculation results for $w(P)$ are shown in Fig. 6. Although w is large 351
at 0.1 MPa (phonolite: 75 kJ/mol, basalt: 85 kJ/mol, and albite: 95 kJ/mol), 352
for all three chemical compositions it monotonically decreases rapidly with 353
increasing pressure over the entire pressure range. This behavior is consistent 354
with the fact that the mutual dissolution of silicate and water proceeds at 355
higher pressures at a fixed temperature, which narrows the miscibility gap. 356

5. Discussion 357

5.1. Can spinodal decomposition occur during decompression-induced 358 vesiculation of magma? 359

First, I focus on the pressure range approximately below 300 MPa, where 360
almost all decompression experiments have been conducted. All nucleation 361
pressure values in 88 previous experiments, from Gardner et al. (1999) to 362

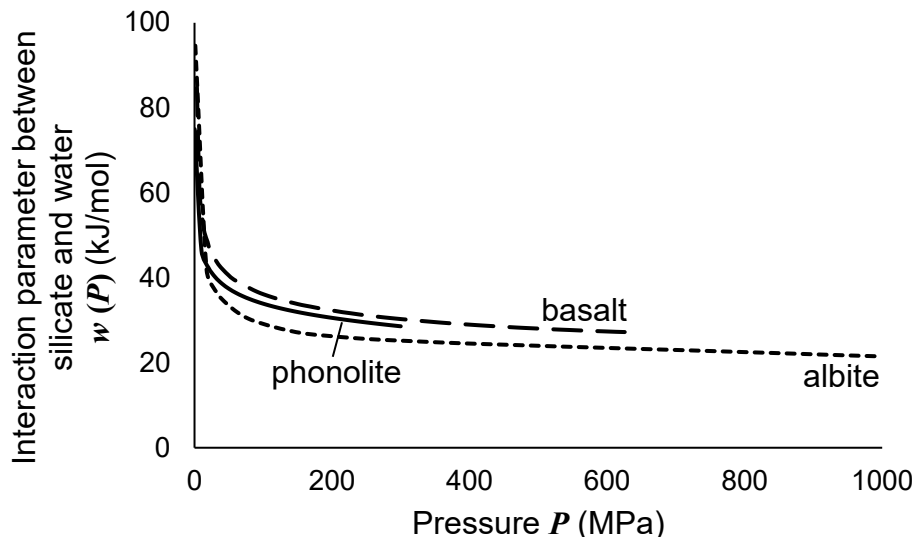


Figure 6: Calculation results of the interaction parameter between silicate and water $w(P)$ for hydrous K-phonolitic melt at 1,050°C and 0.1–300 MPa (solid line), basaltic melt at 1,100°C and 0.1–625 MPa (dashed line), and albite melt at 900°C and 0.1–1000 MPa (dotted line).

Le Gall and Pichavant (2016), compiled and calculated by Shea (2017), fall 363
 within the nucleation region shown in Fig. 5 if variations in melt chemical 364
 composition are not considered. Additionally, all Allabar and Nowak (2018) 365
 experimental runs were performed in the range of the initial pressure of 366
 200 MPa to final pressures of 70–110 MPa. Since the final pressures are 367
 higher than P_{spi} , the nucleation pressure of these runs inevitably falls into 368
 the nucleation region. Therefore, the innovative scenario proposed by Allabar 369
 and Nowak (2018) and Sahagian and Carley (2020)—spinodal decomposition 370
 during decompression-induced vesiculation of magma—cannot occur in the 371
 pressure range of magmatic processes in the continental crust at depths of 372
 several hundred MPa. In addition, since $P_{spi} \ll P_{bi}$ as shown in Fig. 5, 373

for spinodal decomposition to occur without nucleation, it is necessary to 374
maintain sufficient supersaturation, despite a very large decompression from 375
an initial pressure higher than P_{bi} to a pressure lower than P_{spi} . Gardner 376
et al. (2023) stated that we must consider the overlap of various bubble 377
formation mechanisms, including spinodal decomposition, to interpret BND 378
and bubble size distributions in natural pyroclasts, I argue that we can focus 379
only on homogeneous and heterogeneous nucleation as previously envisaged. 380
Note that to confirm indeed that spinodal decomposition is unlikely to 381
occur, it would likely be necessary to conduct runs with relatively rapid 382
decompression to pressures lower than P_{spi} . However, rapid decompression 383
to near atmospheric pressure increases the possibility of capsule rupture, 384
and bubbles' rapid expansion and coalescence may drastically overwrite 385
the geometric arrangement of vesicular textures from its original state. 386
Additionally, as mentioned in 2.3, in some natural systems where degassing is 387
primarily driven by heating rather than decompression, the effective amount 388
of decompression may become larger, making it possible that spinodal 389
decomposition cannot be completely ruled out. 390

On the other hand, in regions of higher pressure and higher water 391
content outside the drawn area of Fig. 5, P_{spi} asymptotically approaches 392
 P_{bi} , and spinodal decomposition is more likely to occur. In other words, 393
spinodal decomposition may occur if decompression passes near the top of the 394
second critical endpoint. In addition, because the second critical endpoint 395
of silicate–water systems has been reported to shift to lower temperatures 396

and pressures with increasing amounts of alkali metal oxides (e.g., Na₂O 397
and K₂O) in the silicate (Bureau and Keppler, 1999; Sowerby and Keppler, 398
2002), Allabar and Nowak (2018) suggested that spinodal decomposition 399
at low pressures may be more likely to occur in alkali-rich phonolite melts 400
than in other silicic silicates. However, as long as the symmetric regular 401
solution approximation is assumed, the shift of the second critical endpoint 402
to lower pressures, i.e., the shift of the binodal curve to lower pressures, is 403
accompanied by a shift of the spinodal curve to lower pressures because 404
 x_{bi} and x_{spi} change in tandem, as shown in Fig. 3. In this case, the 405
region of spinodal decomposition shown in Fig. 5 would be narrower, 406
and spinodal decomposition would be less likely to occur. Therefore, if 407
spinodal decomposition occurs in the phonolitic melt, the binodal curve 408
of the phonolite–water system is expected to have a highly asymmetric 409
shape to which the symmetric regular solution approximation cannot be 410
applied. This might be related to the effective ionic radius of potassium 411
(1.38 Å) that is abundant in the phonolitic melt and is as large as that of 412
oxygen (1.40 Å) (Shannon, 1976). The packing ratio is higher than that in 413
alkali-poor silicates (e.g., albite and rhyolite). Still, the shape of the binodal 414
curve of the phonolite–water system has yet to be determined and requires 415
exploration in detail using high-temperature and high-pressure experiments 416
in the future. Considering additional complexities not accounted for in the 417
symmetric model used in this study, it is difficult to rule out the possibility 418
of spinodal decomposition completely. 419

5.2. Consideration of kinetic effects

420

The discussions in the previous sections were based on equilibrium thermodynamics; thus, static binodal and spinodal curves were determined. However, in reality, during phase separation associated with pressure changes, kinetic effects arise due to the differences in the dynamic properties of silicate and water. As a consequence, the positions of the dynamic binodal and spinodal curves do not coincide with those of the static ones.

421

422

423

424

425

426

Wang et al. (2021) conducted an in-situ observation of the phase separation process of peralkaline aluminosilicate ($\text{Na}_3\text{AlSi}_5\text{O}_{13}$)–water system in a single-phase supercritical fluid near the second critical endpoint (approximately 700°C and 1 GPa) using a hydrothermal diamond anvil cell. As a result, they observed that, at specific composition ratios (37–51 wt% aluminosilicate), the network of hydrous silicate melt emerged as the temperature decreased, and two phases separated, with aqueous fluid enclosed within the silicate melt (spinodal decomposition). Additionally, Raman spectroscopy data collected in situ revealed that polymerized aluminosilicate species were selectively incorporated into the silicate melt, while silica monomers were selectively incorporated into the aqueous fluid. They interpreted this phenomenon by referring to the viscoelastic phase separation (VPS) theory for polymer solutions (Tanaka, 1994), suggesting that the relatively large molecules of the silicate polymer and the small molecules of water have significantly different relaxation timescales, i.e., viscoelastic properties, and thus, they undergo phase separation in a

427

428

429

430

431

432

433

434

435

436

437

438

439

440

441

442

network-like structure. 443

Their experimental results using a peralkaline composition could offer 444
a new perspective in interpreting the experimental results of Allabar and 445
Nowak (2018), which also employed alkali-rich phonolite. Contrary to 446
the traditional image of spinodal decomposition (the so-called “intertwined 447
structure” shown in Fig. 2), the experimental observation that phase 448
separation occurs in a network-like structure suggests that the inference made 449
from the experimental observations in Allabar and Nowak (2018)—where the 450
spatial distribution of bubbles appeared to follow a specific wavelength and 451
was attributed to spinodal decomposition—may not hold. 452

According to Wang et al. (2021), at constant pressure, the dynamic 453
spinodal curve shifts to lower temperatures compared to the static one, as 454
shown in (1) of Fig. 7, where the spinodal curve was drawn with the negative 455
slope, assuming that it would be similar to the negative slope of the phase 456
boundary (binodal curve) appearing in the T – P plane at a fixed composition. 457
In this case, at a fixed temperature, the spinodal curve shifts to the lower 458
pressure side: (2) in Fig. 7. In other words, if the kinetic effects observed 459
in their experiments were to appear in an isothermal decompression system, 460
they would likely occur at pressures lower than the static spinodal pressure 461
 P_{spi} determined from thermodynamic calculations. However, as discussed in 462
the previous section, within the pressure–composition (water content) range 463
where decompression experiments have been conducted, P_{spi} is very low and 464
lower than all the final pressures. Therefore, the scenario proposed by Allabar 465

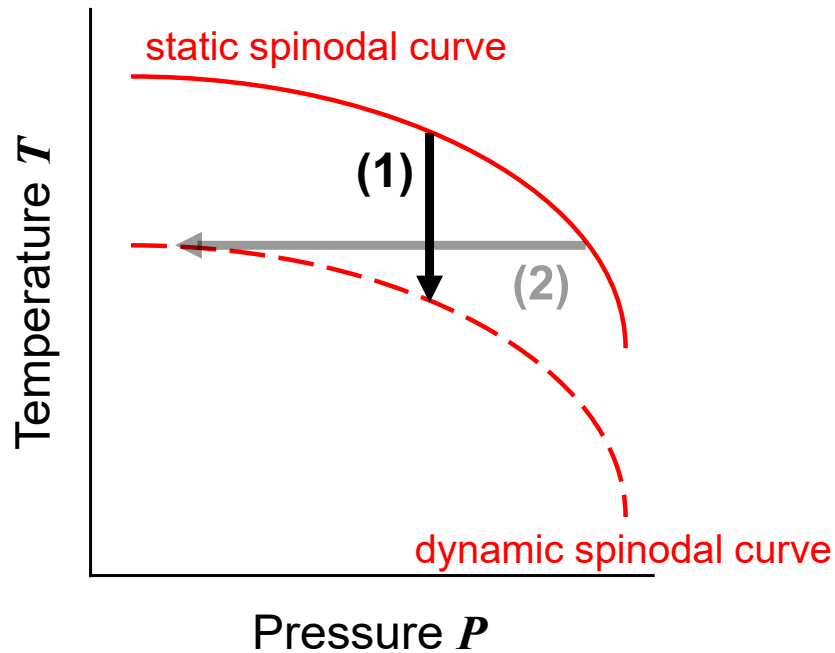


Figure 7: The schematic relationship between the static and dynamic spinodal curves on the T - P plane for a fixed composition. (1) At constant pressure, the dynamic spinodal curve shifts to the lower temperature side compared to the static one (Wang et al., 2021). (2) In this case, at a fixed temperature, the spinodal curve shifts to the lower pressure side.

and Nowak (2018) would be even less likely to occur.

466

5.3. On the compilation of decompression-experimental results

467

Allabar and Nowak (2018) plotted their newly obtained experimental data and selected data from previous decompression experiments (Iacono-Marziano et al., 2007; Marxer et al., 2015; Preuss et al., 2016) conducted under the same chemical composition and physical conditions (phonolitic melt, 1,050°C, initial pressure 200 MPa, and continuous decompression) on the decompression rate-BND plane (see Fig. 8 in their

468

469

470

471

472

473

paper). The BND values of those data were all in the same order of 474
magnitude, almost independent of the decompression rate. In other words, 475
these data are non-harmonic with the classical nucleation theory’s numerical 476
prediction: $\text{BND} \propto |\text{decompression rate}|^{1.5}$ (BND decompression rate meter 477
from Toramaru, 2006). The authors considered that spinodal decomposition, 478
rather than nucleation, might be occurring to explain these experimental 479
results. 480

The selection criteria for past data were not described in Allabar and 481
Nowak (2018) but were detailed in Allabar et al. (2020a, b). In those studies, 482
vesicle shrinkage during cooling and the initial water content dependence 483
of BND in hydrous phonolitic melt were thoroughly investigated through 484
precisely repeated experiments. They revealed that the several factors, 485
denoted in [Appendix B](#), are essential in decompression experiments to 486
determine BND. Only the data obtained under these protocols (hereafter 487
referred to as the “good protocols”) are considered worth discussing in terms 488
of consistency with the BND decompression meter (Allabar et al., 2020b). 489
Though the good protocols were established through a series of experiments 490
using phonolitic melt, since each is based on rational reasoning, they should 491
be applied when conducting experiments with other compositions in the 492
future. 493

I replotted all the experimental data on phonolitic melt at 1,050°C, 494
initial pressure 200 MPa, and continuous decompression in Fig. 8. Here, 495
in addition to the four papers mentioned earlier, data from Allabar et al. 496

(2020b) Table 2 are referenced. The data that meet the good protocols 497
are represented by plots with thick borders. As discussed in Allabar et 498
al. (2020b), since BND has an initial water content dependence, there is 499
some vertical variation even within populations of high BND values, but the 500
variation is smaller compared to the data that mostly do not meet the good 501
protocols from Iacono-Marziano et al. (2007) and Marxer et al. (2015). Even 502
though Marxer et al. (2015)'s data does not satisfy the good protocols, it 503
is harmonic with the BND decompression rate meter. Additionally, several 504
previous papers reported harmonic results with the BND decompression rate 505
meter (e.g., Mourtada-Bonnefoi and Laporte, 2004; Hamada et al., 2010), 506
but they also seem not to satisfy the good protocols. In summary, there 507
is a peculiar inconsistency where some data that do not satisfy the good 508
protocols are in harmony with the BND decompression rate meter, while 509
data that do satisfy the good protocols are not. I suspect that there are 510
two main possible causes for this inconsistency. The first possibility, as 511
mentioned in 5.1, is the uniqueness of the composition of phonolitic melt. It 512
would be worth investigating how the BND decompression rate dependency 513
behaves in the rhyolitic melt, which has relatively low alkali content and 514
a wealth of past experimental examples when conducted following the good 515
protocols. The second possibility, already discussed by Allabar et al. (2020b), 516
is that the potential for heterogeneous nucleation on the surfaces of nanolites 517
or ultrananolites such as Fe–Ti oxides (e.g., Mujin and Nakamura, 2014) 518
cannot be excluded entirely. If the number density of such oxide crystals is 519

a significant control factor for BND, then the BND obtained in experiments 520
may not necessarily follow the BND decompression rate meter. 521

It might also be worth considering how to explain the independence 522
of BND on the decompression rate without using spinodal 523
decomposition—specifically, developing a new CNT-based theory, which 524
could encompass this phenomenon, by improving the BND decompression 525
rate meter. Assuming that all the experimental results plotted in Fig. 8 526
are equally reliable, they suggest that the decompression rate dependence 527
of BND in phonolitic melts is extremely varied. It is known from magma 528
crystallization experiments that the crystal number density can depend on 529
the cooling rate (proportional to the $3/2$ power of the cooling rate; consistent 530
with the CNT-based prediction assuming diffusion-limited growth) as in 531
Toramaru (2001) or shows no dependence, or even decreases (Martel and 532
Schmidt, 2003; Cichy et al., 2011; Andrews and Befus, 2020). Toramaru and 533
Kichise (2023) proposed that this wide range of cooling rate dependence can 534
be explained by varying the pre-exponential factor of the nucleation rate 535
and the surface tension. If there were a bubble version of this crystallization 536
model, it might be possible to explain the wide variety of decompression 537
rate dependence of BND (Toramaru, 2025). 538

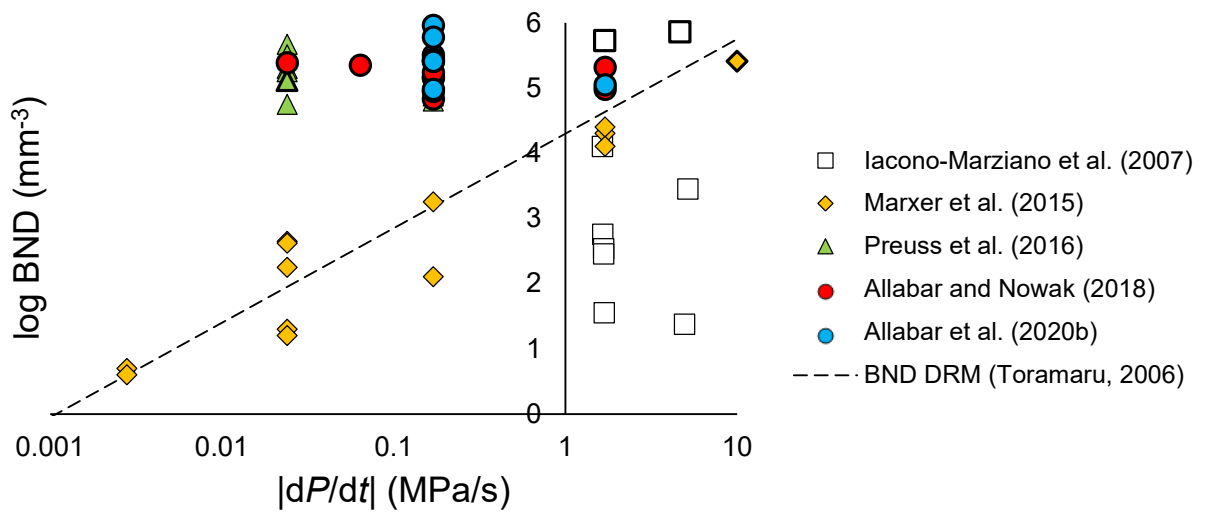


Figure 8: Results of decompression experiments using hydrous K-phonolitic melt from previous works (Iacono-Marziano et al., 2007; Marxer et al., 2015; Preuss et al., 2016; Allabar and Nowak, 2018; Allabar et al., 2020b). The dotted line is the theoretical prediction calculated by BND decompression rate meter, bubble number density decompression rate meter, from Toramaru (2006). The plots with thick borders represent reliable experimental data that meet the “good protocols” for decompression experiments (refer to the main text) described in Allabar et al. (2020b).

5.4. *Application: Estimation of the surface tension between the melt and* 539
bubble nucleus 540

When quantitatively considering the time evolution of the initial stage 541
of magma vesiculation, values for several physical parameters (e.g., diffusion 542
coefficient of water in the melt, viscosity of the melt, and surface tension 543
between the melt and bubble nucleus) are required, as in the case of the BND 544
decompression rate meter by Toramaru (2006). Many of these parameters 545
have been carefully determined through past experiments. Still, even though 546
the “microscopic” surface tension between the melt and (homogeneous 547
spherical) bubble nucleus, σ , is a powerful parameter governing nucleation, its 548
direct measurement is currently impossible. Therefore, it has been calculated 549
only by fitting the integral value of the CNT-based nucleation rate J over 550
time with the obtained BND from decompression experiments: the inversion 551
of BND using the CNT formula (e.g., Mourtada-Bonnefoi and Laporte, 2004; 552
Cluzel et al., 2008; Hamada et al., 2010). However, since the detailed time 553
evolution of J is unknown, σ has not been determined with high precision, 554
and considerable uncertainty exists (Shea, 2017). See [Appendix A](#) for 555
the detailed expression of the equation of J in CNT (e.g., Hirth et al., 556
1970). It has been found that σ obtained via the CNT formula tends to 557
be significantly smaller than the “macroscopic” surface tension σ_∞ at the 558
flat interface between the melt and vapor, directly measured by Bagdassarov 559
et al. (2000) (e.g., Hamada et al., 2010). 560

The reason why $\sigma < \sigma_\infty$ occurs was interpreted by Gonnermann and 561

Gardner (2013) as follows. According to the recent non-classical nucleation theory, the interface between the original and new phases loses sharpness and diffuses under non-equilibrium conditions (e.g., Chapter 4 in Kelton and Greer, 2010). Such interfacial diffusion should also occur during the vesiculation of magma with supersaturated water, which is no longer soluble due to decompression. In other words, the relationship $\sigma = \sigma_\infty$ (capillary approximation) holds at the binodal pressure P_{bi} , but as the supersaturation increases, σ is expected to decrease, and when the spinodal pressure P_{spi} is reached, where a distinct interface is expected to vanish, σ should become zero. They formulated this idea and derived σ using a completely different approach from the BND inversion through CNT. However, at that time, P_{spi} was unknown, so it was considered a hypothetical parameter, and the uncertainty was incorporated into the mathematical treatment. In this study, although a highly simplified equilibrium thermodynamic model is used, P_{spi} was determined for the first time. By substituting this into the equation for the dependence of σ on the degree of supersaturation, the estimation of σ is expected to be improved to a more straightforward way (Nishiwaki, in prep.).

6. Conclusions

I calculated the positions of the binodal and spinodal curves on the chemical composition–pressure plane by assuming that hydrous magma is a two-component symmetric regular solution of silicate and water and using the

chemical thermodynamic equation and experimental data on water solubility 584
in magma. The spinodal curve located significantly lower-pressure side than 585
the binodal curve at pressures sufficiently below the second critical endpoint. 586
The pressure ranges of all previous decompression experiments fell between 587
these two curves. Therefore, decompression-induced vesiculation of magma 588
occurs through nucleation, and spinodal decomposition is highly unlikely, 589
in the magmatic processes associated with volcanic eruptions in most 590
natural continental crusts. This result contradicts the recent inference that 591
spinodal decomposition can occur based on observations of the bubble texture 592
of decompression-experimental products. Additionally, by combining the 593
spinodal pressure determined in this study with the non-classical nucleation 594
theory, it may be possible to easily estimate the surface tension between the 595
silicate melt and bubble nucleus, which has not been accurately determined. 596

Appendix A. Equation of the nucleation rate in classical 597 nucleation theory (CNT) 598

The equation for J in CNT (Hirth et al., 1970) is as follows: 599

$$J = \frac{2n_0^2 D_{\text{H}_2\text{O}} \bar{V}_{\text{H}_2\text{O}}}{a_0} \sqrt{\frac{\sigma}{k_B T}} \exp \left\{ -\frac{16\pi\sigma^3}{3k_B T} (P_B^* - P_M) \right\}, \quad (\text{A.1})$$

where n_0 is the number of water molecules per unit volume, $D_{\text{H}_2\text{O}}$ is the 600
diffusivity of total water in the melt, $\bar{V}_{\text{H}_2\text{O}}$ is the partial molar volume of 601
water in the melt, a_0 is the average distance between water molecules in 602

the melt, σ is the “microscopic” surface tension between the melt and the 603
bubble nucleus, k_B is the Boltzmann’s constant, T is the temperature, P_B^* is 604
the internal pressure of the critical bubble nucleus, and P_M is the pressure of 605
the melt. 606

Appendix B. “Good protocols” established through a series of 607 decompression experiments using phonolitic melt 608

Based on the results of a series of decompression experiments conducted 609
using phonolitic melt (Iacono-Marziano et al., 2017; Marxer et al., 2015; 610
Preuss et al., 2016; Allabar and Nowak, 2018; Allabar et al., 2020b), Allabar 611
et al. (2020b) proposed that ideal experimental products can be obtained 612
by following the protocols outlined below: (a) Homogeneous, bubble-free 613
glass cylinders should be used as starting materials, encapsulated in noble 614
metal tubes containing water for hydration at slightly H_2O undersaturated 615
superliquidus conditions. This setup prevents the presence of fluid bubbles 616
before decompression. (b) The sample should be continuously decompressed 617
at a reasonable decompression time scale to mitigate the drainage of dissolved 618
 H_2O from the melt volume into heterogeneously formed vesicles at the capsule 619
wall. This approach helps to prevent the potential detachment and movement 620
of heterogeneously nucleated vesicles from the capsule walls into the melt 621
volume. (c) To determine the initial BND, the decompression should be 622
terminated at a reasonable final pressure to avoid bubble coalescence which 623
would reduce the initial BND. (d) To determine bubble growth and the onset 624

of bubble coalescence and to observe a possible second bubble formation 625
event, a comprehensive set of experiments with small steps in final pressure 626
down to low pressure is necessary. (e) Subsequent quench of the partially 627
degassed sample should be as fast as possible to minimize vesicle shrinkage. 628
A cooling rate of $\sim 44^\circ\text{C}/\text{s}$ limits bubble shrinkage, inhibits quench crystal 629
formation and avoids the formation of tension cracks. 630

Acknowledgments 631

The author would like to thank Marcus Nowak for sharing numerous 632
detailed and insightful comments on the experiments and results from 633
their team, which significantly contributed to the improvement of the 634
manuscript. The author is grateful to Yosuke Yoshimura for discussing 635
spinodal decomposition in gas–liquid systems induced by pressure changes. 636
The author also appreciates Atsushi Toramaru for his insightful comments 637
on the similarity to the latest crystallization models, which contributed 638
to enhancing the content of this paper. Special thanks go to Takeshi 639
Ikeda for many discussions on the fundamentals of the thermodynamics of 640
silicate–water immiscibility. The reading circle for a glass science text with 641
Shigeru Yamamoto inspired the author for this study. Shumpei Yoshimura 642
provided the author with some methods for calculating the mole fraction of 643
water in magma. The content of this paper was deepened after the discussion 644
with Hidemi Ishibashi and Takayuki Nakatani. The manuscript has been 645
significantly improved through MP and Mathieu Colombier’s peer review, as 646

well as the generous handling by Editor Chiara Maria Petrone. This work 647
was supported by JSPS KAKENHI Grant Number JP23K19069. The author 648
would like to thank Editage (www.editage.jp) for English language editing. 649

References 650

Allabar, A., and Nowak, M., 2018. Message in a bottle: Spontaneous 651
phase separation of hydrous Vesuvius melt even at low decompression rates. 652
Earth Planet. Sci. Lett. **501**, 192–201. [https://doi.org/10.1016/j.
epsl.2018.08.047](https://doi.org/10.1016/j.epsl.2018.08.047) 654

Allabar, A., Dobson, K. J., Bauer, C. C., and Nowak, M., 2020a. Vesicle 655
shrinkage in hydrous phonolitic melt during cooling. *Contrib. Mineral.
Petro.* **175** (3), 21. <https://doi.org/10.1007/s00410-020-1658-3> 657

Allabar, A., Salis Gross E., and Nowak, M., 2020b. The effect of initial 658
H₂O concentration on decompression-induced phase separation and degassing 659
of hydrous phonolitic melt. *Contrib. Mineral. Petro.* **175** (3), 22. [https:
//doi.org/10.1007/s00410-020-1659-2](https://doi.org/10.1007/s00410-020-1659-2) 661

Andrews, B. J., and Befus, K. S., 2020. Supersaturation nucleation 662
and growth of plagioclase: a numerical model of decompression-induced 663
crystallization. *Contrib. Mineral. Petro.* **175** (3), 23. [https://doi.org/
10.1007/s00410-020-1660-9](https://doi.org/10.1007/s00410-020-1660-9) 665

Aursand, P., Gjennestad, M. A., Aursand, E., Hammer, M., and 666
Wilhelmsen, Ø., 2017. The spinodal of single- and multi-component fluids 667
and its role in the development of modern equations of state. *Fluid Phase* 668

Equilib. **436**, 98–112. <https://doi.org/10.1016/j.fluid.2016.12.018> 669

Bagdassarov, N., Dorfman, A., and Dingwell, D. B., 2000. Effect of 670
alkalis, phosphorus, and water on the surface tension of haplogranite melt. 671
Am. Mineral. **85** (1), 33–40. <https://doi.org/10.2138/am-2000-0105> 672

Bureau, H., and Keppler, H., 1999. Complete miscibility between silicate 673
melts and hydrous fluids in the upper mantle: experimental evidence and 674
geochemical implications. *Earth Planet. Sci. Lett.* **165** (2), 187–196. 675
[https://doi.org/10.1016/S0012-821X\(98\)00266-0](https://doi.org/10.1016/S0012-821X(98)00266-0) 676

Burnham, C. W., and Jahns, R. H., 1962. A method for determining 677
the solubility of water in silicate melts. *Am. J. Sci.* **260** (10), 721–745. 678
<https://doi.org/10.2475/ajs.260.10.721> 679

Cahn, J. W., 1965. Phase separation by spinodal decomposition in 680
isotropic systems. *J. Chem. Phys.* **42** (1), 93–99. <https://doi.org/10.1063/1.1695731> 681
682

Cahn, J. W., and Hilliard, J. E., 1959. Free energy of a nonuniform 683
system. III. Nucleation in a two-component incompressible fluid. *J. Chem.* 684
Phys. **31** (3), 688–699. <https://doi.org/10.1063/1.1730447> 685

Cassidy, M., Manga, M., Cashman, K., and Bachmann, O., 2018. 686
Controls on explosive-effusive volcanic eruption styles. *Nat. Commun.* **9** 687
(1), 1–16. <https://doi.org/10.1038/s41467-018-05293-3> 688

Charlier, B., and Grove, T. L., 2012. Experiments on liquid immiscibility 689
along tholeiitic liquid lines of descent. *Contrib. Mineral. Petrol.* **164**, 27–44. 690
<https://doi.org/10.1007/s00410-012-0723-y> 691

Cichy, S. B., Botcharnikov, R. E., Holtz, F., and Behrens, H., 2011. 692
Vesiculation and microlite crystallization induced by decompression: a case 693
study of the 1991–1995 Mt Unzen eruption (Japan). *J. Petrol.* **52** (7–8), 694
1469–1492. [https://doi.org/10.1093/](https://doi.org/10.1093/petrology/egq072) 695
[petrology/egq072](https://doi.org/10.1093/petrology/egq072)

Clemens, J. D., and Navrotsky, A., 1987. Mixing properties of NaAlSi₃O₈ 696
melt–H₂O: new calorimetric data and some geological implications. *J. Geol.* 697
95 (2), 173–188. <https://doi.org/10.1086/629118> 698

Cluzel, N., Laporte, D., Provost, A., and Kannevischer, I., 2008. Kinetics 699
of heterogeneous bubble nucleation in rhyolitic melts: implications for the 700
number density of bubbles in volcanic conduits and for pumice textures. 701
Contrib. Mineral. Petrol. **156** (6), 745–763. [https://doi.org/10.1007/](https://doi.org/10.1007/s00410-008-0313-1) 702
[s00410-008-0313-1](https://doi.org/10.1007/s00410-008-0313-1) 703

Debenedetti, P. G., 2000. Phase separation by nucleation and by spinodal 704
decomposition: Fundamentals. In: Kiran, E., Debenedetti, P. G., Peters, 705
C. J. (Eds.), *Supercritical Fluids*. Nato Science Series **366**, 123–166. 706
https://doi.org/10.1007/978-94-011-3929-8_5 707

Gardner, J. E., Hilton, M., and Carroll, M. R., 1999. Experimental 708
constraints on degassing of magma: isothermal bubble growth during 709
continuous decompression from high pressure. *Earth Planet. Sci. Lett.* **168** 710
(1–2), 201–218. [https://doi.org/10.1016/S0012-821X\(99\)00051-5](https://doi.org/10.1016/S0012-821X(99)00051-5) 711

Gardner, J. E., Wadsworth, F. B., Carley, T. L., Llewelin, E. W., 712
Kusumaatmaja, H., and Sahagian, D., 2023. Bubble formation in magma. 713
Annu. Rev. Earth Planet. Sci. **51**, 131–154. <https://doi.org/10.1146/> 714
<https://doi.org/10.1146/>

[annurev-earth-031621-080308](#)

715

Giachetti, T., Druitt, T. H., Burgisser, A., Arbaret, L., and Galven, C.,
2010. Bubble nucleation, growth and coalescence during the 1997 Vulcanian
explosions of Soufrière Hills Volcano, Montserrat. *J. Volcanol. Geotherm.
Res.* **193** (3–4), 215–231. [https://doi.org/10.1016/j.jvolgeores.
2010.04.001](https://doi.org/10.1016/j.jvolgeores.2010.04.001)

716

717

718

719

720

Gonnermann, H. M., and Gardner, J. E., 2013. Homogeneous bubble
nucleation in rhyolitic melt: Experiments and nonclassical theory. *Geochem.
Geophys. Geosyst.* **14** (11), 4758–4773. [https://doi.org/10.1002/ggge.
20281](https://doi.org/10.1002/ggge.20281)

721

722

723

724

Guggenheim, E. A., 1952. Mixtures: the theory of the equilibrium
properties of some simple classes of mixtures solutions and alloys. Clarendon
Press.

725

726

727

Haasen, P., 1996. Physical metallurgy. Cambridge university press.

728

Hamilton, D. L., Burnham, C. W., and Osborn, E. F., 1964. The
solubility of water and effects of oxygen fugacity and water content on
crystallization in mafic magmas. *J. Petrol.* **5** (1), 21–39. [https://doi.
org/10.1093/petrology/5.1.21](https://doi.org/10.1093/petrology/5.1.21)

729

730

731

732

Hirth, J. P., Pound, G. M., and St Pierre, G. R., 1970. Bubble nucleation.
Metall. Trans. **1** (4), 939–945. <https://doi.org/10.1007/BF02811776>

733

734

Houghton, B. F., Carey, R. J., Cashman, K. V., Wilson, C. J., Hobden,
B. J., and Hammer, J. E., 2010. Diverse patterns of ascent, degassing, and
eruption of rhyolite magma during the 1.8 ka Taupo eruption, New Zealand:

735

736

737

evidence from clast vesicularity. *J. Volcanol. Geotherm. Res.* **195** (1), 738
31–47. <https://doi.org/10.1016/j.jvolgeores.2010.06.002> 739

Hummel, F., Marks, P. L., and Nowak, M., 2024. Preparatory 740
experiments to investigate the vesicle formation of hydrous lower Laacher 741
See phonolite at near liquidus conditions. EGU General Assembly 742
2024, Vienna, Austria, EGU24-19758. [https://doi.org/10.5194/](https://doi.org/10.5194/egusphere-egu24-19758) 743
[egusphere-egu24-19758](https://doi.org/10.5194/egusphere-egu24-19758) 744

Iacono-Marziano, G., Schmidt, B. C., and Dolfi, D., 2007. Equilibrium 745
and disequilibrium degassing of a phonolitic melt (Vesuvius AD 79 “white 746
pumice”) simulated by decompression experiments. *J. Volcanol. Geotherm.* 747
Res. **161** (3), 151–164. [https://doi.org/10.1016/j.jvolgeores.2006.](https://doi.org/10.1016/j.jvolgeores.2006.12.001) 748
[12.001](https://doi.org/10.1016/j.jvolgeores.2006.12.001) 749

James, P. F., 1975. Liquid-phase separation in glass-forming systems. *J.* 750
Mater. Sci. **10**, 1802–1825. <https://doi.org/10.1007/BF00554944> 751

Kakuda, Y., Uchida, E., and Imai, N., 1994. A new model of the excess 752
Gibbs energy of mixing for a regular solution. *Proc. Jpn. Acad. B* **70** (10), 753
163–168. <https://doi.org/10.2183/pjab.70.163> 754

Kennedy, G. C., 1962. The upper three-phase region in the system 755
SiO₂–H₂O. *Am. J. Sci.* **260**, 501–521. [https://doi.org/10.2475/AJS.](https://doi.org/10.2475/AJS.260.7.501) 756
[260.7.501](https://doi.org/10.2475/AJS.260.7.501) 757

Lavallée, Y., Dingwell, D. B., Johnson, J. B., Cimarelli, C., Hornby, A. 758
J., Kendrick, J. E., von Aulock, F. W., Kennedy, B. M., Andrews, B. J., 759
Wadsworth, F. B., Rhodes, E., and Chigna, G., 2015. Thermal vesiculation 760

during volcanic eruptions. *Nature* **528** (7583), 544–547. <https://doi.org/10.1038/nature16153>

Le Gall, N., and Pichavant, M., 2016. Homogeneous bubble nucleation in H₂O- and H₂O–CO₂- bearing basaltic melts: Results of high temperature decompression experiments. *J. Volcanol. Geotherm. Res.* **327**, 604–621. <https://doi.org/10.1016/j.jvolgeores.2016.10.004>

Makhluf, A. R., Newton, R. C. and Manning, C. E., 2020. Experimental investigation of phase relations in the system NaAlSi₃O₈–H₂O at high temperatures and pressures: Liquidus relations, liquid-vapor mixing, and critical phenomena at deep crust-upper mantle conditions. *Contrib. Mineral. Petrol.* **175** (8), 76. <https://doi.org/10.1007/s00410-020-01711-2>

Marks, P. L., and Nowak M., 2024. Decoding the H₂O phase separation mechanism as the trigger for the explosive eruption of the Lower Laacher See phonolite. EGU General Assembly 2024, Vienna, Austria, EGU24-7723. <https://doi.org/10.5194/egusphere-egu24-7723>

Martel, C., and Schmidt, B. C., 2003. Decompression experiments as an insight into ascent rates of silicic magmas. *Contrib. Mineral. Petrol.* **144** (4), 397–415. <https://doi.org/10.1007/s00410-002-0404-3>

Marxer, H., Bellucci, P., and Nowak, M., 2015. Degassing of H₂O in a phonolitic melt: A closer look at decompression experiments. *J. Volcanol. Geotherm. Res.* **297**, 109–124. <https://doi.org/10.1016/j.jvolgeores.2014.11.017>

Moore, G., Vennemann, T., and Carmichael, I. S. E., 1998. An empirical

model for the solubility of H₂O in magmas to 3 kilobars. *Am. Mineral.* **83** 784
(1–2), 36–42. <https://doi.org/10.2138/am-1998-1-203> 785

Mujin, M., and Nakamura, M., 2014. A nanolite record of eruption style 786
transition. *Geology* **42** (7), 611–614. <https://doi.org/10.1130/G35553.1> 787

Murase, T., and McBirney, A. R., 1973. Properties of some common 788
igneous rocks and their melts at high temperatures. *Geol. Soc. Am. Bull.* **84** 789
(11), 3563–3592. [https://doi.org/10.1130/0016-7606\(1973\)84<3563:
POSCIR>2.0.CO;2](https://doi.org/10.1130/0016-7606(1973)84<3563:POSCIR>2.0.CO;2) 790
791

Nguyen, C. T., Gonnermann, H. M., and Houghton, B. F., 2014. 792
Explosive to effusive transition during the largest volcanic eruption of the 793
20th century (Novarupta 1912, Alaska). *Geology* **42** (8), 703–706. <https://doi.org/10.1130/G35593.1> 794
795

Nishiwaki, M., 2023. Chemical-thermodynamic explorations on the 796
dissolution of water in magma: Breaking of the ideal mixing model 797
and estimations of temperature change with decompression-induced 798
vesiculation. Doctoral Dissertation, Kyushu University. [https://catalog.lib.kyushu-u.ac.jp/opac_detail_md/?reqCode=frombib&
lang=0&amode=MD823&opkey=B168673756684664&bibid=6787423&start=
1&bbinfo_disp=0](https://catalog.lib.kyushu-u.ac.jp/opac_detail_md/?reqCode=frombib&lang=0&amode=MD823&opkey=B168673756684664&bibid=6787423&start=1&bbinfo_disp=0) 799
800
801
802

Paillat, O., Elphick, S. C., and Brown, W. L., 1992. The solubility of 803
water in NaAlSi₃O₈ melts: a re-examination of Ab–H₂O phase relationships 804
and critical behaviour at high pressures. *Contrib. Mineral. Petrol.* **112**, 805
490–500. <https://doi.org/10.1007/BF00310780> 806

Preuss, O., Marxer, H., Ulmer, S., Wolf, J., and Nowak, M., 2016. 807
Degassing of hydrous trachytic Campi Flegrei and phonolitic Vesuvius 808
melts: Experimental limitations and chances to study homogeneous bubble 809
nucleation. *Am. Mineral.* **101** (4), 859–875. [https://doi.org/10.2138/](https://doi.org/10.2138/am-2016-5480) 810
[am-2016-5480](https://doi.org/10.2138/am-2016-5480) 811

Richet, P., Hovis, G., and Whittington, A., 2006. Water and magmas: 812
Thermal effects of exsolution. *Earth Planet. Sci. Lett.* **241** (3–4), 972–977. 813
<https://doi.org/10.1016/j.epsl.2005.10.015> 814

Richet, P., Hovis, G., Whittington, A., and Roux, J., 2004. Energetics 815
of water dissolution in trachyte glasses and liquids. *Geochim. Cosmochim.* 816
Acta **68** (24), 5151–5158. <https://doi.org/10.1016/j.gca.2004.05.050> 817

Sahagian, D., and Carley, T. L., 2020. Explosive volcanic eruptions and 818
spinodal decomposition: A different approach to deciphering the tiny bubble 819
paradox. *Geochem. Geophys. Geosyst.* **21** (6), e2019GC008898. <https://doi.org/10.1029/2019GC008898> 820
<https://doi.org/10.1029/2019GC008898> 821

Shannon, R. D., 1976. Revised effective ionic radii and systematic 822
studies of interatomic distances in halides and chalcogenides. *Acta* 823
Crystallogr. A: Found. Adv. **32** (5), 751–767. [https://doi.org/10.1107/](https://doi.org/10.1107/S0567739476001551) 824
[S0567739476001551](https://doi.org/10.1107/S0567739476001551) 825

Shea, T., 2017. Bubble nucleation in magmas: A dominantly 826
heterogeneous process?. *J. Volcanol. Geotherm. Res.* **343**, 155–170. 827
<https://doi.org/10.1016/j.jvolgeores.2017.06.025> 828

Shen, A. H., and Keppler, H., 1997. Direct observation of complete 829

miscibility in the albite–H₂O system. *Nature* **385** (6618), 710–712. <https://doi.org/10.1038/385710a0>

Shimozuru, D., Nakamura, O., Seno, H., Noda, H., and Taneda, S., 1957. Mechanism of pumice formation. *Bull. Volcanol. Soc. Japan* **2**, 17–25.

Sowerby, J. R., and Keppler, H., 2002. The effect of fluorine, boron and excess sodium on the critical curve in the albite–H₂O system. *Contrib. Mineral. Petrol.* **143** (1), 32–37. <https://doi.org/10.1007/s00410-001-0334-5>

Sparks, R. S. J., 1978. The dynamics of bubble formation and growth in magmas: A review and analysis. *J. Volcanol. Geotherm. Res.* **3** (1–2), 1–37. [https://doi.org/10.1016/0377-0273\(78\)90002-1](https://doi.org/10.1016/0377-0273(78)90002-1)

Stolper, E., 1982a. Water in silicate glasses: An infrared spectroscopic study. *Contrib. Mineral. Petrol.* **81** (1), 1–7. <https://doi.org/10.1007/BF00371154>

Stolper, E., 1982b. The speciation of water in silicate melts. *Geochim. Cosmochim. Acta* **46** (12), 2609–2620. [https://doi.org/10.1016/0016-7037\(82\)90381-7](https://doi.org/10.1016/0016-7037(82)90381-7)

Tanaka, H., 1994. Critical dynamics and phase-separation kinetics in dynamically asymmetric binary fluids: New dynamic universality class for polymer mixtures or dynamic crossover?. *J. Chem. Phys.* **100** (7), 5323–5337. <https://doi.org/10.1063/1.467197>

Toramaru, A., 1989. Vesiculation process and bubble size distributions in ascending magmas with constant velocities. *J. Geophys. Res. Solid Earth*

94 (B12), 17523–17542. <https://doi.org/10.1029/JB094iB12p17523> 853

Toramaru, A., 1995. Numerical study of nucleation and growth of bubbles 854
in viscous magmas. *J. Geophys. Res. Solid Earth* **100** (B2), 1913–1931. 855
<https://doi.org/10.1029/94JB02775> 856

Toramaru, A., 2001. A numerical experiment of crystallization for a 857
binary eutectic system with application to igneous textures. *J. Geophys.* 858
Res. Solid Earth **106** (B3), 4037–4060. [https://doi.org/10.1029/](https://doi.org/10.1029/2000JB900367) 859
[2000JB900367](https://doi.org/10.1029/2000JB900367) 860

Toramaru, A., 2006. BND (bubble number density) decompression rate 861
meter for explosive volcanic eruptions. *J. Volcanol. Geotherm. Res.* **154** 862
(3–4), 303–316. <https://doi.org/10.1016/j.jvolgeores.2006.03.027> 863

Toramaru, A., 2022. Vesiculation and crystallization of magma: 864
Fundamentals of volcanic eruption process, conditions for magma 865
vesiculation. Springer Singapore. [https://doi.org/10.1007/](https://doi.org/10.1007/978-981-16-4209-8) 866
[978-981-16-4209-8](https://doi.org/10.1007/978-981-16-4209-8) 867

Toramaru, A., 2025. The theoretical basis for textural indices of eruption 868
dynamics: review and new conceptual models. *Earth Planets Space* **77**, 27. 869
<https://doi.org/10.1186/s40623-025-02146-4> 870

Toramaru, A., and Kichise, T., 2023. A new model of crystallization 871
in magmas: Impact of pre-exponential factor of crystal nucleation rate on 872
cooling rate exponent and log-linear crystal size distribution. *J. Geophys.* 873
Res. Solid Earth **128** (10), e2023JB026481. [https://doi.org/10.1029/](https://doi.org/10.1029/2023JB026481) 874
[2023JB026481](https://doi.org/10.1029/2023JB026481) 875

Verhoogen, J., 1951. Mechanism of ash formation. *Am. J. Sci.* **249**, 723–739.

Wang, Q. X., Zhou, D. Y., Li, W. C., and Ni, H. W., 2021. Spinodal decomposition of supercritical fluid forms melt network in a silicate–H₂O system. *Geochem. Perspect. Lett.* **18**, 22–26. <https://doi.org/10.7185/geochemlet.2119>

Zhang, Y., 1999. H₂O in rhyolitic glasses and melts: measurement, speciation, solubility, and diffusion. *Rev. Geophys.* **37** (4), 493–516. <https://doi.org/10.1029/1999RG900012>

CRedit authorship contribution statement

Mizuki Nishiwaki: Conceptualization, Methodology, Formal analysis, Investigation, Writing – Original Draft, Writing – Review & Editing, Visualization, Project administration, Funding acquisition.

Declaration of competing interest

The author declares that he has no known competing financial interests or personal relationships that could have appeared to influence the work reported in this paper.

Data availability

The author confirms that the data supporting the findings of this study are available within the article.

Table 1: Notation list.

Symbol	Unit	Definition
a_0	m	Average distance between water molecules in the melt
c	no unit	Water solubility in the melt (mole fraction)
$D_{\text{H}_2\text{O}}$	$\text{m}^2 \text{s}^{-1}$	Diffusivity of total water in the melt
g^{excess}	J mol^{-1}	Molar excess Gibbs energy for a regular solution
g^{ideal}	J mol^{-1}	Molar Gibbs energy of an ideal solution
g^{real}	J mol^{-1}	Molar Gibbs energy of mixing ($= g^{\text{ideal}} + g^{\text{excess}}$)
h^{excess}	J mol^{-1}	Molar excess enthalpy for a non-ideal solution
J	$\text{No m}^{-3} \text{s}^{-1}$	Nucleation rate
k_{B}	J K^{-1}	Boltzman's constant
n_0	No m^{-3}	Number of water molecules per unit melt volume
P	Pa	Pressure
P_{bi}	Pa	Pressure on the binodal curve (= binodal pressure)
P_{spi}	Pa	Pressure on the spinodal curve (= spinodal pressure)
P_{M}	Pa	Melt pressure
P_{SAT}	Pa	Water saturation pressure
P_{B}^*	Pa	Internal pressure of the critical bubble nucleus
R	$\text{J K}^{-1} \text{mol}^{-1}$	Gas constant
s^{excess}	$\text{J K}^{-1} \text{mol}^{-1}$	Molar excess entropy for a non-ideal solution (= 0 for a regular solution)
T	K	Temperature
$\bar{V}_{\text{H}_2\text{O}}$	$\text{m}^3 \text{mol}^{-1}$	Partial molar volume of water in the melt
w_{sym}	J mol^{-1}	Interaction parameter between two components for a symmetric regular solution
$w_{\text{A,B}}$	J mol^{-1}	Interaction parameter between two components for an asymmetric regular solution
w_{ijk}	J mol^{-1}	Interaction parameter between three components for an asymmetric regular solution
X	no unit	Symbolic notation for chemical composition
x	no unit	Mole fraction of one of the two components
$x_{\text{bi}}(P)$	no unit	The x that constitutes the binodal curve at pressure P
$x_{\text{spi}}(P)$	no unit	The x that constitutes the spinodal curve at pressure P
σ	N m^{-1}	“Microscopic” surface tension between the melt and homogeneous spherical bubble nucleus with a large curvature
σ_{∞}	N m^{-1}	“Macroscopic” surface tension at the flat interface between the melt and vapor